Simultaneous X-ray and Visible Light Quantitative Imaging for Multiphase Flow

R. R. La Foy*, E. M. Hall, and B. R. Halls
Sandia National Laboratory
Albuquerque, NM, 87123, United States of America

Abstract

Often features of a multiphase flow may be obscured in visible light or effectively transparent to X-ray light. However, combining these two imaging techniques may offer a more complete description of the underlying dynamics. To investigate the combination of these techniques, both X-ray and visible light high-speed camera systems with non-overlapping fields-of-view recorded a flow field consisting of gases, particulates, and fragments travelling between approximately 100 and 250 m/s that were generated from an explosive device. The fragments were first recorded by a camera imaging a scintillator that was illuminated by an array of eight 150 kV flash X-ray sources firing sequentially. Next, two high-speed cameras in a stereo configuration imaged the fragment motion with visible light approximately one meter downstream. Camera calibration data was combined with the fragment motion video to calculate the fragment geometries and three-dimensional positions as functions of time. Then the fragments were matched between the X-ray and visible light data by performing a nearest-neighbor search of the parametric space consisting of the fragment diameters, speeds, trajectories, and origin points. Matches were found with a high degree of confidence, successfully demonstrating the ability to quantitatively image a multi-phase flow simultaneously with both X-ray and visible light systems.

*Corresponding author: rrlafoy@sandia.gov

Introduction

Characterizing the dynamics of the high-speed motion of metallic fragments is critical to many applications including in the design of energetic devices, defining safety requirements, and completing forensic analysis. Previous work has used both visible light and x-ray imaging to record the fragment dynamics [1], [2], [3], [4], however due to the limitations of both techniques, they are typically record dynamics in different regions of the flow-field. Additionally, some work has recorded experimental data of energetic devices specifically to validate simulations [5].

X-ray imaging is particularly suitable for imaging the flow-field near energetic devices where the release of energy in the form a fireball can saturate visible light cameras and the high density of aerosolized particulates obscures optical access to the ejected fragments. An X-ray imaging system is not sensitive to the visible light released by the fireball and the X-ray light can typically pass through the particulates with little attenuation. Conversely, metallic fragments released during the detonation tend to have a high absorption of X-rays and thus can be recorded with relatively high contrast.

There are two primary limitations with X-ray imaging of energetic devices. First, since the velocity of the fragments tends to be relatively high – on the order of hundreds of meters per second – using a continuous X-ray source would result in significant blurring in the recorded images due to the motion of the fragments. Thus, high-speed flash X-ray sources must be used. These sources can only be fired once per test shot, therefore the number of recorded frames is limited to the number of available sources. Second, the scintillators used in high-speed applications such as this tend have very low spatial resolution with low contrast, resulting in images with low signal-to-noise ratios.

In contrast to this, images recorded using visible light imaging tend to have both high spatial and temporal resolution and the number of recorded frames is typically only limited by the buffer of the high-speed camera. This means that in the far-field region outside of the fireball, visible light cameras are ideally suited for recording the fragment dynamics since high-precision position data can be recorded across a large number of time-resolved frames.

Since the regions that X-ray and visible light imaging systems are optimally suited to work within tend to be different, the fields of view of the imaging systems generally do not overlap. For this reason, this work focuses on collecting measurements with both an X-ray system and a visible light system and shows that these measurements can produce consistent results. Specifically, an energetic device was used to generate a high-speed fragmentation event in which both flash X-ray and visible light image sequences were recorded and fragments that were imaged by both systems were parametrically matched.

Experimental Setup

The experimental setup imaging system was divided into the X-ray camera system and the visible light stereo camera system. The explosive device was placed near the edge of the field-of-view of the X-ray imaging system and oriented so that a ring of fragments would be generated that expanded across the imaging system fields-of-view. The ring first traversed the X-ray imaging field-of-view and then later extended across the visible imaging system approximately 1 m downstream. The X-ray and visible light cameras were synced together and recorded at a frame rate of 25 kHz.

The X-ray imaging system was placed within a steel camera box to protect the equipment from damage during the tests. The system consisted of one Phantom TMX 7510 camera imaging the X-ray scintillator using a Zeiss Milvus 25 mm lens with the aperture set to f/1.4 at a focal distance of approximately 40 cm. The scintillator was a Scintacor Rapidex Bright screen that was cut to approximately 30 cm by 30 cm in size and clamped into place over the viewing window of the camera box. This screen decays to 10% of the initial intensity in about 7 μs, so there was little residual signal from previous frames that were at least 40 μs before. A sheet of 0.25 inch thick polycarbonate was placed directly in front of the scintillator to protect the screen from damage due to the high-speed fragments. The resultant X-ray images tended to be relatively noisy and have low resolution compared to the visible light images.

The flash X-ray tubes were L3Harris Technologies 150 keV sources with 3 mm nominal anode spot sizes mounted in two horizontal rows in an approximately hexagonal grid with the top row containing five tubes and the bottom containing four. During the experiments the last tube on the top row ceased firing, so most data was collected with only eight operational tubes. The tubes were spaced approximately 10 cm apart center-to-center and were angled slightly so that they were all pointing towards the center of the scintillator screen. The distance from the tubes to the screen was about 52 cm. A 0.5 inch thick sheet of polycarbonate was placed 8 cm in front of the X-ray tubes to protect them from damage.

Two Phantom v2512 high-speed cameras were used for the stereo visible imaging system. The cameras both had Canon EF 24 to 70 mm zoom lenses attached that were focused to a distance of 70 cm with the zoom focal length set to 50 mm and with the aperture equal to f/11.0. The first camera was centered approximately 80 cm from the explosive device while the second camera was at a distance of 100 cm. The two cameras were angled inward by approximately 15 degrees between them to maximize the overlapping fields-of-view. A polycarbonate box with 0.5 inch thick walls was placed over the cameras to shield them from damage. The scene that the cameras imaged was backlit with three high intensity continuous LED lights that were diffused through a 0.125 inch polycarbonate sheet. The diffuser sheet was placed approximately 0.9 m in front of the cameras.

The tests were conducted with an explosive bridgewire RP-80 detonator that was placed inside a 3D-printed plastic case that was surrounded by a 1.37 inch diameter aluminum ring. The device was mounted on an optical breadboard using a set screw that connected an optical post to the 3D-printed case. During the tests, the majority of the imaged fragments consisted of portions of the aluminum ring that were between approximately 0.5 and 2.0 cm in length. Some small steel fragments from the detonator case are also apparent in the images. A total of eight shots were completed in this preliminary experiment.

Camera Calibration

Imaging systems used to record three-dimensional tracking data are calibrated to relate the recorded image coordinates to the world coordinates of the tracked objects. The calibration procedure produces a function that relates the world coordinates to the image coordinates for each imaging system. Then given the image coordinates of an object that is seen by multiple cameras, the three-dimensional coordinates can be determined by inverting these calibration functions. For simple calibration functions, this inversion can be calculated analytically. However, in real world systems the camera calibration is typically too complex to be analytically inverted, so an optimum solution is typically calculated by minimizing some residual error.

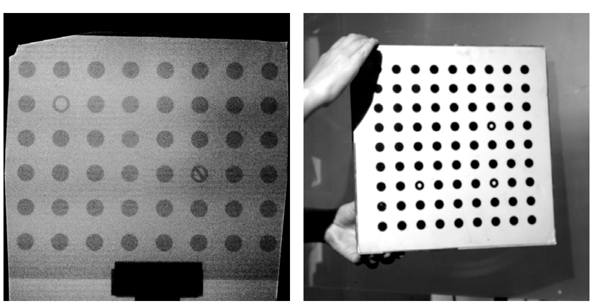

(a) **(b)**

Figure 1. This shows example calibration images from the X-ray system (a) and the visible light system (b). The post for accurately positioning the X-ray calibration grid can be seen in the bottom of the image and is in contrast to the arbitrary placement of the grid by the experimenter in the visible light image. Additionally, the relatively low quality of the X-ray images in comparison to the visible light images can be seen in these images.

Given a set of image coordinates, these functions yield a curve through world space whose points all map to that set of image coordinates. This effectively gives the line-of-sight for these image coordinates. Estimating the three-dimensional coordinates of an object effectively corresponds to a triangulation procedure in which the approximate intersections of these lines-of-sight curves is found.

The calibration process of the experimental system was broken down into two separate procedures; one for the X-ray system that is based upon a generalized cubic polynomial model and another for the visible light cameras that used the commercial VIC-3D software by Correlated Solutions [6] that uses a pinhole model with high-order lens distortions included [7]. The two calibrations were performed using grids optimized for each camera system.

The X-ray camera system, which requires one calibration for each X-ray flash tube, was calibrated by moving a grid of copper circles printed on a PCB board through the imaging volume. The PCB board attenuated the X-ray image intensity by approximately 4% while the regions of the PCB board that included the copper cladding attenuated the intensity by about 10%. This difference is sufficiently high for the position of the copper circles could be accurately calculated in the images. The circles had diameters of 15 mm and were spaced 30 mm apart in a rectilinear pattern. The grid was translated in 1 inch increments by moving an optical post across an optical breadboard. An example calibration image is shown in Figure 1a in which the low resolution, low contrast nature of the X-ray imaging system is apparent.

The X-ray calibration images were first normalized by brightfield images that were recorded without any imaged objects to ensure that the intensity was approximately uniform across the images. Then the sub-pixel image coordinates (x, y) of the grid circles were calculated in each image using the built-in MATLAB function 'imfindcircles' that is based upon a Circular Hough Transform algorithm [8] [9]. A different set of image coordinates were calculated for each flash X-ray source. The world coordinates of the grid points (X, Y, Z) were defined by the relative locations of the circles on the PCB board along with the position on the optical breadboard. This then yielded a unique set of (x, y, X, Y, Z) calibration coordinates for each of the eight X-ray sources.

The coordinates were then fit to third order polynomial calibration functions of the form

$$x = \sum_{i=0}^{3}\sum_{j=0}^{3}\sum_{k=0}^{3} \alpha_{ijk} X^i Y^j Z^k \ni \ i + j + k \leq 3 \qquad (1)$$

$$y = \sum_{i=0}^{3}\sum_{j=0}^{3}\sum_{k=0}^{3} \beta_{ijk} X^i Y^j Z^k \ni\ i+j+k \leq 3 \qquad (2)$$

using a least squares regression. A different calibration function (corresponding to a different set of coefficients α_{ijk} and β_{ijk}) was calculated for the data generated by each flash X-ray source, producing eight different calibration functions. The three-dimensional coordinates of imaged objects were calculated by finding the set of world coordinates that minimized the difference between the evaluated calibration functions and the measured image coordinates.

The visible light cameras were calibrated using a rectilinear grid comprised of black circles printed onto a white background that was translated and rotated into various orientations in front the two cameras. The pinhole calibration procedure only requires that the grid of points be planar in each frame, so the calibration grid was manually moved throughout the imaging volume by an experimenter. Several thousand frames of data were recorded by each camera during the calibration procedure. The grid points were 1.5 cm in diameter and spaced 3.0 cm apart. An image demonstrating the manual orientation of the calibration grid and the higher quality of the visible light images is shown in Figure 1b. The calibration function calculation was performed using the VIC-3D software and exported to MATLAB for the fragment tracking.

Since the X-ray and visible light calibration procedures yielded independent coordinate systems, a two-step process was applied to the resultant calibration functions to ensure that both camera systems were operating in the same coordinate frame. The first step involved defining a new coordinate system and calculating a translation offset from the original X-ray coordinate system. Only a single point was used to define the new coordinate system, therefore, the rotation with the original coordinate system could not be uniquely defined and was set equal to zero for simplicity. Then in the second step, the coordinates of several grid points on the copper calibration grid that were in view of the visible light camera system were calculated in the new coordinate system. These grid points were then used to transform the original visible light coordinate system into new coordinate system by defining both a translation and a rotation that was then applied.

The center of the aluminum ring surrounding the detonator was defined as the origin of the new coordinate system since this was the physical origin of the fragments and could be easily imaged by the X-ray camera system. During the dynamic tests, the optical post supporting the device was moved such that the device was mostly outside the field-of-view of the X-ray system. However, the post was translated 2.0 inches towards the direction of the fragment motion for calibration, corresponding to a positive X direction, and static X-ray images were collected. In this translated position, the device could be imaged by all eight of the X-ray flash imaging systems. The center of the aluminum ring was found in each image using a similar circle finding algorithm to that used for the calibration grids. These image coordinates were then used to estimate the three-dimensional world coordinate of the center of the ring. Then, the origin of the new coordinate system was defined as the location 2.0 inches in the negative X direction and the X-ray calibration functions were translated such that this new position now corresponded to the origin.

The copper calibration grid extended into the visible camera imaging field-of-view, so the visible camera calibration functions could be adjusted by defining the new three-dimensional coordinates of at least three non-colinear visible grid points and then determining the translations and rotations necessary to ensure the visible camera calibration functions match these coordinates. In practice, the world coordinates of the grid points were calculated in the original coordinate system using the calibration inversion triangulation procedure and then the translation vector and rotation matrix were calculated that transformed the original coordinates to the new coordinates. These transformations were then applied to the original visible light camera calibration functions to yield the new calibration functions.

X-Ray Attenuation Calibration

Ideally, three-dimensional tracking algorithms yield the center of mass of the tracked objects since this is the ideal reference frame for calculating forces acting upon the objects. In visible light imaging, the center of mass is often approximated by the image centroid of the object. However, the location of the center of mass can be directly calculated for X-ray images to within the imaging uncertainty. This is accomplished by calculating an intensity attenuation curve and then inverting this function to generate images that directly give the pathlength that the X-rays passed through of the imaged objects. The centroids of the objects in these images will then give the center of mass of the objects.

To calculate the attenuation curves, calibration images of objects with known thicknesses ΔZ are collected, these images are normalized by brightfield images containing no objects (so the intensity scales between zero and one), and the normalized image intensity I_n of the scintillator that results from the different levels of attenuation are measured.

If the X-ray source emitted light at a single frequency and the scintillator and camera responses where perfectly linear, then the attenuation would be governed by the Beer-Lambert law [10] and the image intensity would decrease exponentially with material thickness. However, due to the polychromatic X-ray sources used and non-linearities in the response of the imaging system, it was found that a double exponential of the form

$$I_n(\Delta Z) = a \exp(-b\,\Delta Z) + (1-a)\exp(-c\,\Delta Z) \qquad (3)$$

represented the attenuation curves more closely. The coefficients a, b, and c were calculated by performing a least squares regression with the collected thickness and normalized intensity data.

An example attenuation data set along with fit single and double exponential curves is shown in Figure 2. The single exponential curve can be seen to fit the data more poorly than the double exponential curve represented by Equation 3. Additionally, the single exponential curve does not equal a value of one for zero thickness as is expected.

Since the attenuation function monotonically decreases with material thickness, the function may be inverted to yield the material thickness as a function of the normalized image intensity. Equation 3 cannot be analytically inverted, however, monotonic functions can be easily numerically inverted using root finding algorithms such as Newton's method. Using this method, the X-ray images can be easily converted from the normalized intensity values to pathlength values.

Example normalized intensity and pathlength images from a fragmentation event are shown in Figure 3. The pathlength was calculated assuming that the imaged materials were all aluminum. This is correct for the large fragments, however the small fragments on the outer edge of the expanding ring are steel fragments from the detonator case and due to the higher density, incorrectly appear to have long pathlengths. The image coordinates of the center of mass of the individual fragments can now be determined by calculating the centroids of the fragments in the pathlength image. Note that the correct material attenuation curve must be chosen for this calculation to be accurate.

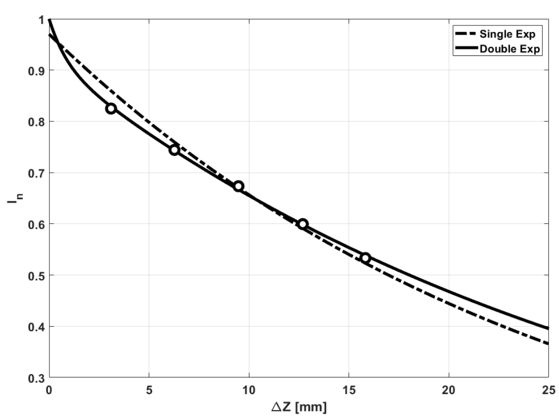

Figure 2. This graph illustrates the necessity of using a double exponential function to model the X-ray attenuation curves. The black circles and solid lines correspond to the measured attenuation data and fit double exponential curves respectively. The dotted line represents the same data fit to a Beer-Lambert single exponential.

(a) **(b)**

Figure 3. These images show an example fragmentation event with both the normalized intensity image (a) and the estimated pathlength image (b). In the normalized intensity image, the intensity corresponds to the X-ray irradiance and thus denser or thicker objects appear darker. The intensity in the pathlength image is proportional to the thickness of the imaged objects and thus thicker objects appear brighter.

Fragment Tracking

The three-dimensional world coordinates of the fragments were determined by first calculating the image coordinates of the fragments and then estimating the world coordinates that these image coordinates corresponded to using the triangulation procedure discussed earlier. Since the visible light cameras recorded all frames simultaneously, this process was relatively straightforward as long as the same fragment could be identified in both camera images. However, since the X-ray images were all recorded at different time instances, a different procedure was used that relied upon the motion of the fragments to estimate their position in each frame.

Since only eight frames of X-ray data were recorded in each shot, relatively few fragments were visible in the X-ray images, and the X-ray images were low resolution and noisy, manually tracking the fragments was found to be the most efficient method for segmenting the images. This process consisted of four steps. First, the approximate center of mass of each fragment in the images was selected with the cursor on a computer. Next, the boundary around the fragments was manually drawn with the cursor. Then, the boundary was computationally refined by shifting the points defining the boundary to the location of the maximum absolute value of the image gradient. And finally, the centroid of the pathlength image was calculated within the refined boundary. This procedure was repeated to yield a series of between three

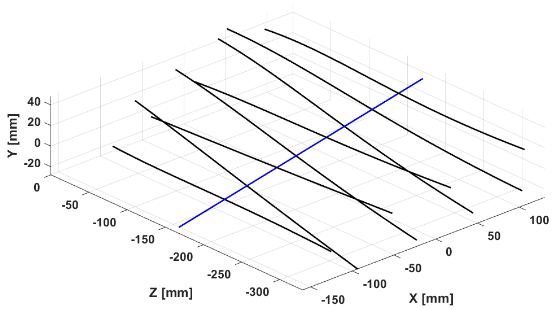

Figure 4. This graph shows the projected lines-of-sight of a tracked fragment from the scintillator to each flash X-ray source (in black) along with the estimated fragment trajectory (in blue). The fragment trajectory can be seen to pass by the line-of-sights at nearly equidistance positions. Note that this is the original X-ray coordinate system and is not centered on the detonator (which would be to the front-left of the graph).

and eight frames of image coordinates for each of the tracked fragments.

Since simultaneous images of the fragments from multiple views were not recorded, it was assumed that the fragment motion was approximately constant within the eight recorded X-ray frames. A constant motion results in the three-dimensional world coordinates of the fragments translating by the same distance and in the same direction between each pair of frames. Then determining the world coordinates of the fragments in the X-ray images corresponds to finding an initial position (X_0, Y_0, Z_0) and a constant velocity (v_X, v_Y, v_Z) that results in image coordinates that most closely match those that were measured for the fragments. Since the initial position and velocity have six degrees of freedom total and each frame of data f has two degrees of freedom from the image coordinates (x_f, y_f), then this means that at least $T = 3$ frames of data are required to yield a unique solution. In cases where the fragment position was measured for $T \geq 3$ frames, this becomes a minimization problem where the goal is to minimize the residual of

$$r = \sum_{f=1}^{T} \sqrt{\left(x_f - {}_fC_x(X_f, Y_f, Z_f)\right)^2 + \left(y_f - {}_fC_y(X_f, Y_f, Z_f)\right)^2} \qquad (4)$$

where ${}_fC_x(X_f, Y_f, Z_f)$ and ${}_fC_y(X_f, Y_f, Z_f)$ are the x and y image coordinate calibration functions of frame f respectively, the fragment world coordinates are given by

$$X_f = X_0 + v_X \cdot t_f \qquad (5)$$
$$Y_f = Y_0 + v_Y \cdot t_f \qquad (6)$$
$$Z_f = Z_0 + v_Z \cdot t_f \qquad (7)$$

and t_f corresponds to the time of frame f. Geometrically, this corresponds to finding a parametric line through three-dimensional space that passes the projected calibration curve lines-of-sight from each fragment image coordinate at approximately equidistant positions. An example fragment trajectory and the associated lines-of-sight is shown in Figure 4.

The visible light fragment images were higher contrast, higher resolution, and were recorded over a significantly longer time period than the X-ray images. This allowed the fragment tracking process to be completely automated. Approximate fragment image positions were calculated by thresholding the images, applying a segmentation algorithm, performing a local refinement of the segmentation, and then calculating the centroids of the segmented regions. This process is described more fully in [11] and [12]. The fragments were then tracked between frames by using a Regression-based Multiframe Tracking algorithm [12] to yield refined image coordinates and to ensure that fragments were properly matched across the frames. Finally, the three-dimensional world coordinates were calculated using a triangulation algorithm within the Vic3D software [6].

Basic geometric information was also calculated and recorded for the tracked fragments in both the X-ray and visible light images. This information included es-

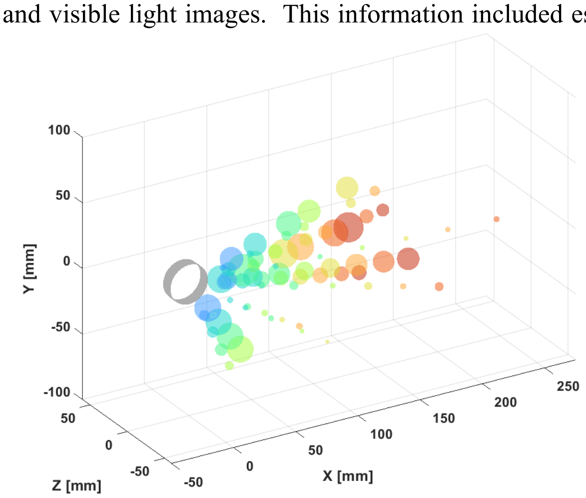

Figure 5. The motion of the fragments tracked in the X-ray system from one detonation case are shown in this graph. The detonator is denoted by the grey cylindrical ring while the colors represent the time instance in which the fragment position was calculated with blue showing the earliest times and red reflecting the latest times. The diameter of colored circles denotes the major-axis dimensions of the fragments and is plotted to scale. The smaller, faster moving fragments are steal ejected from the detonator case while the larger, slower moving fragments correspond to the aluminum ring around the detonator.

timates of the distance across the fragments in the longest or major-axis direction, the width of the fragments in the perpendicular minor-axis direction, and the areas of the fragments that were seen by each imaging system. A plot summarizing the tracking information for the X-ray imaging system for one detonation is shown in Figure 5.

X-Ray and Visible Light Fragment Matching

Once the fragment positions and geometries were determined for both the X-ray and visible light imaging systems, fragments were matched between the two systems. Since there was no overlapping field of view between the systems, the matching process involved extrapolating the trajectories of the fragments and matching these estimated trajectories and the fragment geometries.

Due to the small field of view and low resolution, on the order of approximately ten fragments were typically tracked in the X-ray images. However, the visible light images generally allowed several hundred fragments to be tracked. This meant that there were potentially thousands of possible fragment matches. So, to narrow down the number of possible matches, a parametric nearest neighbor search was completed to match fragments between the X-ray and visible light images.

This matching process involved defining each fragment by a set of eight parameters: the major-axis dimension of the fragment, the mean velocity of the fragment, the three-component direction of the motion of the fragment, and the three-component origin coordinate of the fragment. All parameters were normalized to have zero mean values and standard deviations of approximately one so that the magnitude of the individual parameters would not unduly weight particular parameters more heavily than others. Finally, estimates of the uncertainty on each of the parameters were used to provide weights for each of the parameters. The mean velocity was typically known with a high degree of certainty while the fragment length scale was typically less precisely known due to tumbling for example.

The matching process was completed using a k-d tree nearest neighbor search using the built-in MATLAB function ‘knnsearch’ function [13]. Since there were generally far more fragments in the visible light data than the X-ray data, this meant that typically all X-ray data fragments would be matched to one fragment in the visible light data.

Once potential matches were found using the nearest neighbor parametric search, image sequences of the specific fragments were visually analyzed to ensure that the specific fragment geometries and potential tumbling also matched since these parameters were not specifically accounted for in the parametric search. In some cases, multiple potential fragment matches were visually investigated until a likely match was confirmed.

	X-Ray	Visible
Diameter [mm]:	17.80	14.78
Velocity [m/s]:	260.66	252.39
Trajectory [N/A]:	(0.97, 0.05, 0.22)	(0.98, 0.05, 0.20)
Origin [mm]:	(0.43, -1.79, -0.05)	(39.17, 3.10, -0.86)

Table 1. This table shows the measured non-normalized parameters of one potential fragment match between the X-ray and visible light imaging systems.

Results

While this was a preliminary experiment with only a small number of shots completed, the data confirmed that tracking dynamic events between X-ray and visible light imaging is successful. All test shots yielded likely fragment matches, with several shots producing multiple potential matches. The non-normalized parameters of one potential match are shown in Table 1. The large differences in the magnitudes of these parameters demonstrates the necessity of normalizing the parameters prior to matching since if this step was not completed, the velocity would likely dominate all potential matches due to its much larger magnitude.

Image sequences from both the X-ray and visible light camera systems for the fragment described in Table 1 are shown in Figure 6. While some fragments rapidly rotate, these image sequences show that this fragment only changes orientation by a small amount from one frame to the next lending support to the conclusion that this is a correct fragment match. Additionally, the size and overall shape of the fragment appear to closely match between the X-ray and visible light sequences. Most fragments that were successfully matched had very similar parameters and visual appearances, however,

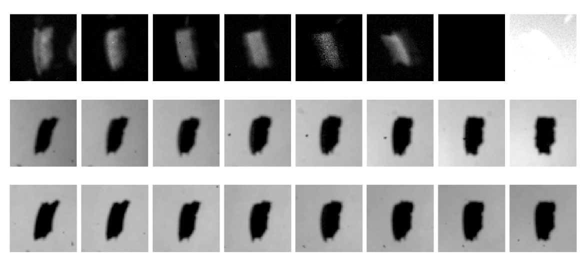

Figure 6. This figure shows a time series of the same matched fragment that is described in Table 1. Images from the X-ray system are shown on the top row, the first stereo visible light camera in the middle row, and the second stereo visible light camera in the bottom row. The X-ray images correspond to frames 3, 5, 7, 9, 11, 13, 15, and 17 while the two visible image sequences correspond to frames 67 to 74. All three image sequences are shown at approximately the same magnification.

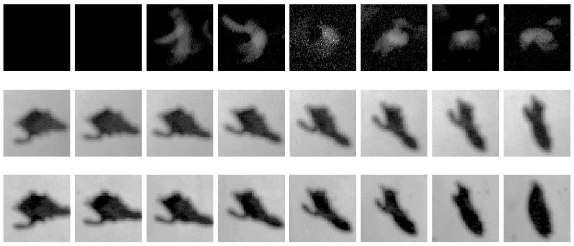

Figure 7. This figure shows the image sequences of a successful fragment match that bounced between the X-ray and visible light imaging times. The X-ray images correspond to frames 3, 7, 11, 15, 19, 23, 27, and 31 while the two visible image sequences correspond to frames 146 to 153.

several unexpected matches were also found.

It was generally assumed that any fragment matches found between the X-ray and visible light imaging systems would require the fragments to only pass through free space between the two systems since any fragments that bounced from a surface between the two imaging systems would have fundamentally different parameters. However, one fragment was successfully matched that appeared to bounce off the front surface of the camera box between being imaged by the X-ray and visible light systems. The parameters describing this fragment were very different, however the fragment motion remained in a roughly horizontal plane between the X-ray and visible light measurements. Additionally, the velocity magnitude of the fragment dropped from 208.4 m/s to 109.0 m/s between the measurements suggesting that when the fragment impacted the camera box, a large portion of the fragment's kinetic energy was absorbed. Due to the large number of fragments involved, this would generally not be sufficient evidence to confirm that this was a correct fragment match, however the fragment had a unique geometry that is shown in the image in Figure 7 that gives significant evidence that the bouncing theory is likely correct. This suggests that more thoroughly characterizing the fragment geometry and rotational motion would likely result in more potential matches.

Conclusions

This work demonstrated a methodology for tracking dynamic objects between X-ray and visible light imaging systems with non-overlapping fields of view. It was found that the low resolution, low contrast nature of flash X-ray imaging required a relatively higher magnification than an equivalent visible light system to perform comparable levels of tracking. Additionally, it was found that measuring multiple parameters that characterize the tracked objects significantly improved the likelihood of finding successful matches between the X-ray and visible light systems.

Further experiments will be completed with a larger number of shots so that statistical data can be drawn from the experiments. Additionally, more advanced methods to characterize the fragment parameters will be developed. Specifically, measuring the full three-dimensional geometry of the fragment as well as estimating the rate and direction of rotation will likely improve matching rates.

Acknowledgements

This paper describes objective technical results and analysis. Any subjective views or opinions that might be expressed in the paper do not necessarily represent the views of the U.S. Department of Energy or the United States Government. Sandia National Laboratories is a multimission laboratory managed and operated by National Technology & Engineering Solutions of Sandia, LLC, a wholly owned subsidiary of Honeywell International Inc., for the U.S. Department of Energy's National Nuclear Security Administration under contract DE-NA0003525.

References

[1] G. Huang and S. Feng, "Axial distribution of Fragment Velocities from cylindrical casing under explosive loading," *International Journal of Impact Engineering,* vol. 76, pp. 20-27, 2015.

[2] Z. Guo, G. Huang, C. Liu and S. Feng, "Velocity axial distribution of fragments from non-cylindrical symmetry explosive-filled casing," *International Journal of Impact Engineering,* vol. 118, pp. 1-10, 2018.

[3] T. Hiroe, K. Fujiwara, H. Hata and H. Takahashi, "Deformation and fragmentation behaviour of exploded metal cylinders and the effects of wall materials, configuration, explosive energy and initiated locations," *International Journal of Impact Engineering,* vol. 35, no. 12, pp. 1578-1586, 2008.

[4] D. Bors, J. Cummins and J. Goodpaster, "Anatomy of a Pipe Bomb Explosion: Measuring the Mass and Velocity Distributions of Container Fragments," *Journal of Forensic Sciences,* vol. 59, no. 1, pp. 42-51, 2014.

[5] D. Guildenbecher, E. Jones, E. Hall, P. Reu, T. Miller, F. Perez, A. Thompson and J. Ball, "3D optical diagnostics for explosively driven deformation," *International Journal of Impact Engineering,* vol. 162, 2021.

[6] "VIC-3D," Correlated Solutions, 2024. [Online]. Available:

https://www.correlatedsolutions.com/vic-3d. [Accessed 19 March 2024].

[7] A. Zisserman and R. Hartley, Multiple View Geometry in Computer Vision, Cambridge University Press, 2004.

[8] T. Atherton and D. Kerbyson, "Size invariant circle detection," *Image and Vision Computing,* vol. 17, no. 11, pp. 795-803, 1999.

[9] H. Yuen, J. Princen, J. Illingworth and J. Kittler, "Comparative study of Hough Transform methods for circle finding," *Image and Vision Computing,* vol. 8, no. 1, pp. 71-77, 1990.

[10] S. Carmignato, W. Dewulf and R. Leach, Industrial X-Ray Computed Tomography, Springer, 2018.

[11] J. Yeager, P. Bowden and D. Guildenbecher, "Characterization of hypervelocity metal fragments for explosive initiation," *Journal of Applied Physics,* vol. 122, 2017.

[12] D. Guildenbecher, M. Cooper and P. Sojka, "High-speed (20 kHz) digital in-line holography for transient particle tracking and sizing in multiphase flows," *Applied Optics,* vol. 55, no. 11, pp. 2892-2903, 2016.

[13] J. Friedman, J. Bentley and R. Finkel, "An Algorithm for Finding Best Matches in Logarithm Expected Time," *ACM Transactions on Mathematical Software,* vol. 3, no. 2, pp. 209-226, 1977.